Materials Horizons

ROYAL SOCIETY OF CHEMISTRY

COMMUNICATION

View Article Online
View Journal | View Issue

Cite this: *Mater. Horiz.*, 2025, 12, 7439

Received 10th April 2025,
Accepted 19th June 2025

DOI: 10.1039/d5mh00658a

rsc.li/materials-horizons

An asymmetrically tipped MoS_2/CdS heterostructure for high-performance photocatalytic plastic reforming†

Yu Yao,[a] Jinqiang Zhang, *[a] Panpan Zhang,[b] Lei Shi,[c] Kunsheng Hu,[a] Tara Pukala, [d] Yanlin Shi, [e] Zhongfan Jia, [e] Shaobin Wang [a] and Xiaoguang Duan *[a]

Photoreforming plastic waste into valuable chemicals while simultaneously splitting water to produce hydrogen (H_2) under mild conditions presents a sustainable strategy to address environmental issues and generate solar fuels. Herein, we report a MoS_2/CdS heterojunction photocatalyst synthesized *via* a one-pot solvothermal method for plastic reforming and H_2 production. The strong Mo–S–Cd interaction at the interface creates a robust internal electric field (IEF), which promotes efficient charge carrier separation. The macroscopic asymmetry of tipping growth of MoS_2 on one end of CdS nanorods further promotes imbalanced charge carriers' distribution and increased charge population. As a result, the IEF and structural asymmetry ensure electron migration from MoS_2 to CdS for proton reduction to yield H_2, leaving oxidative holes in MoS_2 to drive poly(lactic) acid (PLA) reforming. Under visible light irradiation, the catalyst achieved a high H_2 production rate of 97.7 mmol g^{-1} h^{-1} without using cocatalysts or sacrificial agents. Concurrently, MoS_2/CdS converted PLA into lactate and pyruvate. This dual-function catalyst demonstrates exceptional promise for sustainable H_2 production and plastic waste upcycling.

New concepts

In this work, we demonstrate a macroscopically asymmetric, covalently stitched Janus heterojunction in which a few-layer MoS_2 "tip" is epitaxially grown on only one end of a CdS nanorod. The resulting Mo–S–Cd interface generates a robust built-in electric field that bends the bands into an S-scheme, automatically separating photocarriers: electrons migrate to CdS for proton reduction, while holes remain in MoS_2 to oxidise plastic hydrolysates. Unlike conventional symmetric MoS_2/CdS mixtures, core–shells or van der Waals assemblies, this geometry-amplified internal field (i) obviates external bias, cocatalysts or sacrificial agents, (ii) withstands highly alkaline media, and (iii) boosts charge-separation efficiency to a record 97.7 mmol g^{-1} h^{-1} H_2 during visible-light photoreforming of waste polylactic acid, achieving two orders of magnitude above that of state-of-the-art photocatalysts. This concept provides a general design principle for materials science: creating lattice-matched semiconductors through directional covalent junctions and deliberate geometric polarity can embed a "wireless bias" inside the material itself. Such internal-field engineering opens new avenues for solar-powered up-cycling of recalcitrant polymers and solid wastes and other multi-electron redox transformation processes.

1. Introduction

Plastics are extensively used in sectors like food packaging and biomedicine and are valued for their exceptional properties, such as great mechanical strength, lightweight, low toxicity, and versatility, in compositional and property engineering. However, petroleum-based plastics, rich in carbon and hydrogen,[1] pose significant environmental hazards upon improper disposal. Conventional disposal methods, including incineration and landfilling, exacerbate these issues by generating massive greenhouse and toxic gases and producing micro/nanoplastics that directly release or transfer harmful organic pollutants to the ecosystem. Photoreforming (PR) of plastics, coupled with the hydrogen (H_2) evolution reaction (HER), has emerged as a promising alternative pathway *via* upgrading plastic waste into valuable chemicals meanwhile generating H_2 under mild conditions. Nevertheless, the high thermodynamic barriers for separating photo-induced charge carriers (electrons and holes) and extremely acidic or alkaline environments for plastic pre-treatment limit the efficiency of existing photocatalytic systems.[2] This highlights a pressing need for developing highly active and robust photocatalysts capable of

[a] *School of Chemical Engineering, The University of Adelaide, Adelaide, SA 5005, Australia. E-mail: jinqiang.zhang@adelaide.edu.au, xiaoguang.duan@adelaide.edu.au*
[b] *School of Chemistry and Chemical Engineering, Jiangsu University, Zhenjiang 212013, China*
[c] *College of Materials Science and Engineering, Nanjing Forestry University, Nanjing, Jiangsu, 210037, China*
[d] *School of Physics, Chemistry and Earth Sciences, The University of Adelaide, SA 5005, Australia*
[e] *Institute for Nanoscale Science and Technology, College of Science and Engineering, Flinders University, Bedford Park, South Australia 5042, Australia*

† Electronic supplementary information (ESI) available. See DOI: https://doi.org/10.1039/d5mh00658a

maintaining H_2 production performance under challenging conditions and regulating the product selectivity of plastic waste.

Traditional semiconductor photocatalysts encounter challenges such as limited light absorption and sluggish charge dynamics, resulting in slow surface redox kinetics. In this regard, asymmetric composite materials offer notable advantages by creating oriented charge distributions and migration due to the strong polarization at the interface.[3,4] The built-in electrical field (BIEF) remarkably accelerates charge carriers' separation and reduces their recombination, leading to improved photocatalytic activity and higher H_2 yields.[5] However, traditional heterojunction catalysts frequently suffer from energy level mismatches and incoherent hot spots (or active sites) at semiconductor interfaces, limiting solar energy utilization as well as the efficiency and selectivity of surface photoredox reactions.[6–8] In contrast, Janus catalysts overcome these limitations by forming compact and well-defined charge–directional interfaces that minimize energy losses during charge transfer and enhance long-term stability.[9,10] This composite configuration improves charge carrier mobility and accelerates reaction kinetics, resulting in higher redox capabilities.[9,11] Therefore, constructing intimate interfaces and strong BIEF is essential for advancing photocatalytic performances in synergistic plastic reforming and H_2 revolution.

Transition metal chalcogenides (TMCs), recognized for their strong photocatalytic activity, broad visible light absorption, and tunable band gaps,[12,13] hold great promise for solar-driven catalysis. However, their efficiency is often restrained by limited stability due to photo-corrosion[14] and high recombination rates of photoexcited electron–hole pairs. Designing TMC heterojunctions with high lattice matching can improve interfacial charge dynamics and photostability, leading to high activities of plastic PR coupled with the HER. Despite these advantages, existing TMC heterojunctions face some challenges, including complex synthesis methods, weak interfacial interactions and requirement of cocatalysts and sacrificial agents.

Herein, we developed an asymmetric MoS_2/CdS (disulfide/cadmium sulfide) heterojunction catalyst through an *in situ* epitaxial growth strategy to decorate MoS_2 nanoshells on one side of the CdS nanorods. The robust Mo–S–Cd interaction at the dense interface establishes a robust BIEF, creating high-efficiency electron transfer channels to facilitate rapid charge separation and directional charge redistribution, thus minimizing charge carriers' recombination. Experimental and computational findings revealed an S-scheme heterojunction, where electrons migrate from the conduction band (CB) of MoS_2 to the valence band (VB) of CdS for recombination. This process aligns hot electrons and holes in the CB of CdS and VB of MoS_2, ensuring effective spatial charge separation and reduced thermodynamic barriers for enhanced H_2 production and selective plastic reforming. The optimized MoS_2/CdS Janus catalyst achieved efficient proton reduction in CdS, reaching an impressive H_2 production rate of 97.7 mmol g^{-1} h^{-1} under visible light irradiation in KOH-pretreated polylactic acid (PLA) solution, without using any cocatalysts or sacrificial agents. Meanwhile, the holes in MoS_2 facilitated selective PLA oxidation into lactate and pyruvate. Both redox processes outperformed state-of-the-art photocatalysts, demonstrating significant potential for sustainable waste plastic recycling and solar fuel production.

2. Experimental section

2.1 Materials

The following reagents were purchased from Sigma-Aldrich: cadmium nitrate tetrahydrate ($Cd(NO_3)_2{\cdot}4H_2O$), thiourea (NH_2CSNH_2), ethylenediamine, sodium molybdate ($Na_2MoO_4{\cdot}2H_2O$), lactic acid, sodium sulfate (Na_2SO_4), potassium hydroxide (KOH), deuterium oxide (D_2O), triethanolamine, methanol, Nafion solution (5 wt%), polylactic acid (PLA), poly(ethylene terephthalate) (PET), polystyrene (PS), polypropylene (PP), and poly(vinyl chloride) (PVC). Ultra-pure water (18.2 MΩ cm) was obtained from a Milli-Q water purification system and used for all aqueous solutions.

2.2 Synthesis of CdS nanorods

Pure CdS nanorods (NRs) were synthesized using a solvothermal method. In this process, 1.07 g of $Cd(NO_3)_2{\cdot}4H_2O$ and 1.38 g of thiourea (NH_2CSNH_2) were dissolved in 100 mL of ethylenediamine solution with stirring for 30 minutes. The resulting mixture was then transferred to a 150 mL Teflon-lined autoclave and heated at 220 °C for 24 hours. The precipitates were collected by filtration and thoroughly rinsed with deionized water and ethanol. Finally, CdS NRs were obtained after drying at 60 °C for 24 hours.

2.3 Synthesis of *x*-MoS_2 tipped CdS NRs

x-MoS_2/CdS heterojunction photocatalysts were synthesized using a simple one-pot solvothermal method, as illustrated schematically in Fig. S1 (ESI†). Following the procedure outlined above, Na_2MoO_4, $Cd(NO_3)_2{\cdot}4H_2O$, and NH_2CSNH_2 were dissolved in 100 mL of ethylenediamine solution under continuous stirring for 30 minutes. The resulting mixture was then transferred to a 150 mL Teflon-lined autoclave and heated in an oven at 220 °C for 24 hours. To prepare control samples, Na_2MoO_4 was added to the solution at varying weight ratios relative to $Cd(NO_3)_2$: 0.35%, 0.7%, 1.05%, 1.4%, and 1.75%. The resulting photocatalysts were washed twice with ethanol and deionized water, filtered, dried in an oven at 60 °C for 24 hours, and designated as 1-MoS_2/CdS, 2-MoS_2/CdS, 3-MoS_2/CdS, 4-MoS_2/CdS, and 5-MoS_2/CdS, respectively.

2.4 Pre-treatment of PLA, PET, PS, PP and PVC

12 g of PLA, PET, PS, PP, and PVC were separately added to 250 mL of KOH solution (10 M). The mixtures were stirred at 60 °C for 48 hours in an oil bath. Following this hydrolysis process, the resulting solutions were subsequently used as hole scavengers to replace the sacrificial agent during the photocatalytic process.

2.5 Characterization

X-ray powder diffraction (XRD) patterns were collected on a Rigaku MiniFlex 600 X-ray diffractometer. Mo/Cd ratios in the

photocatalysts were measured using an Agilent 8900 triple quadrupole inductively coupled plasma mass spectrometer (ICP-MS). X-ray photoelectron spectroscopy (XPS) spectra were acquired on an Escalab 250XI system (Al Kα X-ray) from Thermo Fisher Scientific. Steady-state photoluminescence (PL) spectra were recorded with an RF-5301PC spectrofluorophotometer (Shimadzu, Japan). High-resolution transmission electron microscopy (HRTEM) images and energy-dispersive X-ray spectroscopy (EDS) spectra were captured using an FEI Titan Themis microscope, equipped with a JEOL 2100F microscope and a high-angle annular dark field (HAADF) detector.

^{1}H NMR spectra were recorded on two different instruments. Quantitative analyses were performed on a Bruker AVANCE III 600 MHz spectrometer (Germany), using maleic acid as the internal standard and D_2O as the solvent. Additional spectra were acquired using a Bruker Ultrashield Plus 600 MHz spectrometer at 298 K. Deuterated solvents were used as internal locks, and the residual D_2O peak (δ = 4.79 ppm) was used as the chemical shift reference. The light absorption characteristics and estimated bandgaps of all samples were analyzed on an Agilent Cary Series 100 UV-vis spectrophotometer. Transient-state photoluminescence (PL) spectra were collected using an FLS1000 spectrometer (Edinburgh Instruments, UK). LC-MS/MS acquisitions were conducted using Xcalibur v2.1 software from Thermo Fisher Scientific, with the mass spectrometer functioning in data-dependent acquisition mode. Femtosecond transient absorption spectroscopy (fs-TAS) measurements were performed using a 360 nm pump pulse and a white-light probe covering the 390–680 nm range. X-ray absorption near-edge structure (XANES) spectra at the Cd and Mo K-edges were collected in fluorescence mode at the soft X-ray spectroscopy beamline of the Australian Synchrotron.

2.6 Photoelectrochemical measurements

All electrochemical and photoelectrochemical measurements were conducted on a CHI 760E workstation using a standard three-electrode system in a 0.5 M sodium sulfate aqueous solution, with a 300 W Xe lamp as the light source. The working electrode was a 10 mm × 10 mm FTO glass slide coated with a slurry containing 5 mg of photocatalysts (CdS, MoS_2, or MoS_2/CdS) and 20 μL of 5 wt% Nafion solution. A Pt foil served as the counter electrode, and Ag/AgCl was used as the reference electrode. Mott–Schottky plots were recorded over a potential range of −2 to −0.2 V *vs.* Ag/AgCl, with an amplitude of 0.01 V and frequencies of 800, 1000, and 1200 Hz.

2.7 Photocatalytic H_2 reaction

The photocatalytic performance of the materials was evaluated in a 250 mL custom-made batch reactor at room temperature and ambient pressure. A 300 W xenon lamp (PLS-SXE 300, Beijing Perfectlight) equipped with a UV-cutoff filter ($\lambda > 420$ nm) provided visible light irradiation. In each photocatalytic test, 5 mg of the catalyst was ultrasonically dispersed in 100 mL of solution. For photocatalytic H_2 evolution from water, the system consisted of 90 mL of deionized water and 10 mL of lactic acid (LA) as a sacrificial agent. For PR of plastic, 100 mL of pretreated PLA, PET, PS, PP, or PVC solution (48 mg mL^{-1}), without any added sacrificial agent, was used. The supernatant obtained after plastic pretreatment was directly employed in the PR reactions. High-purity N_2 gas was purged into the photocatalyst suspension for 30 minutes to eliminate residual air. The reactor was irradiated with continuous stirring for 2 hours, and the generated H_2 was analyzed using an Agilent 490 Micro GC gas chromatograph.

2.8 Theoretical computations

The simulations were conducted using the Vienna ab initio simulation package (VASP), employing the generalized gradient approximation (GGA) for electron exchange–correlation energy and the projected augmented wave (PAW) method to address ion–electron interactions.[15–17] The (002) plane of MoS_2 and (102) plane of CdS were selected to simulate their respective work functions. To construct the CdS(102)/MoS_2(002) interface model, a MoS_2(002) slab was positioned on a CdS(102) slab, with the interfacial lattice mismatch minimized to less than 5% by applying supercells of MoS_2(002) and CdS(102) and introducing a 15 Å vacuum layer in the *z*-direction.[18] The resulting lattice parameters of the CdS(102)/MoS_2(002) interface model were a = 9.741 Å and b = 16.631 Å, with a cutoff energy of 520 eV. Structural relaxation was achieved using the conjugate gradient method with a residual force convergence criterion of 0.03 eV Å^{-1}. The *k*-point meshes applied were 3 × 2 × 1 for structural relaxation and 5 × 3 × 1 for density of states calculations. The work function was determined using the following equation:

$$\Phi = E_{vac} - E_F$$

where E_{vac} and E_F are the electrostatic potential of the vacuum level and the Fermi energy, respectively.[19] The calculation method of H adsorption Gibbs free energy can be found in ref. 20.

3. Results and discussion

We developed a series of asymmetric MoS_2/CdS nanostructured photocatalysts (x-MoS_2/CdS, x = 1–5 for different loading amounts of Na_2MoO_4 precursor) using a one-pot solvothermal approach under mild conditions, as shown in Fig. S1 (ESI†). This method enabled the simultaneous epitaxial growth of MoS_2 and CdS under hydrothermal conditions, featuring MoS_2 formation at one end of CdS nanorods. Unlike traditional methods often requiring intricate procedures and high reaction temperatures,[21,22] this approach affords more cost-effective and scalable synthesis of Janus heterostructures. The asymmetry of one-side-tipped CdS/MoS_2 heterostructures further promoted macroscopic charge-distribution imbalance and population increase upon light irradiation. Moreover, the single-step epitaxial growth creates a denser and more robust interface featuring strong interfacial Mo–S–Cd covalent bonding, which is different from the heterojunctions formed *via* weaker van der Waals interactions.[22–24]

Scanning electron microscopy (SEM) images (Fig. 1a) revealed that the 3-MoS_2/CdS sample exhibited a high-aspect-ratio morphology, characterized by diameters ranging from

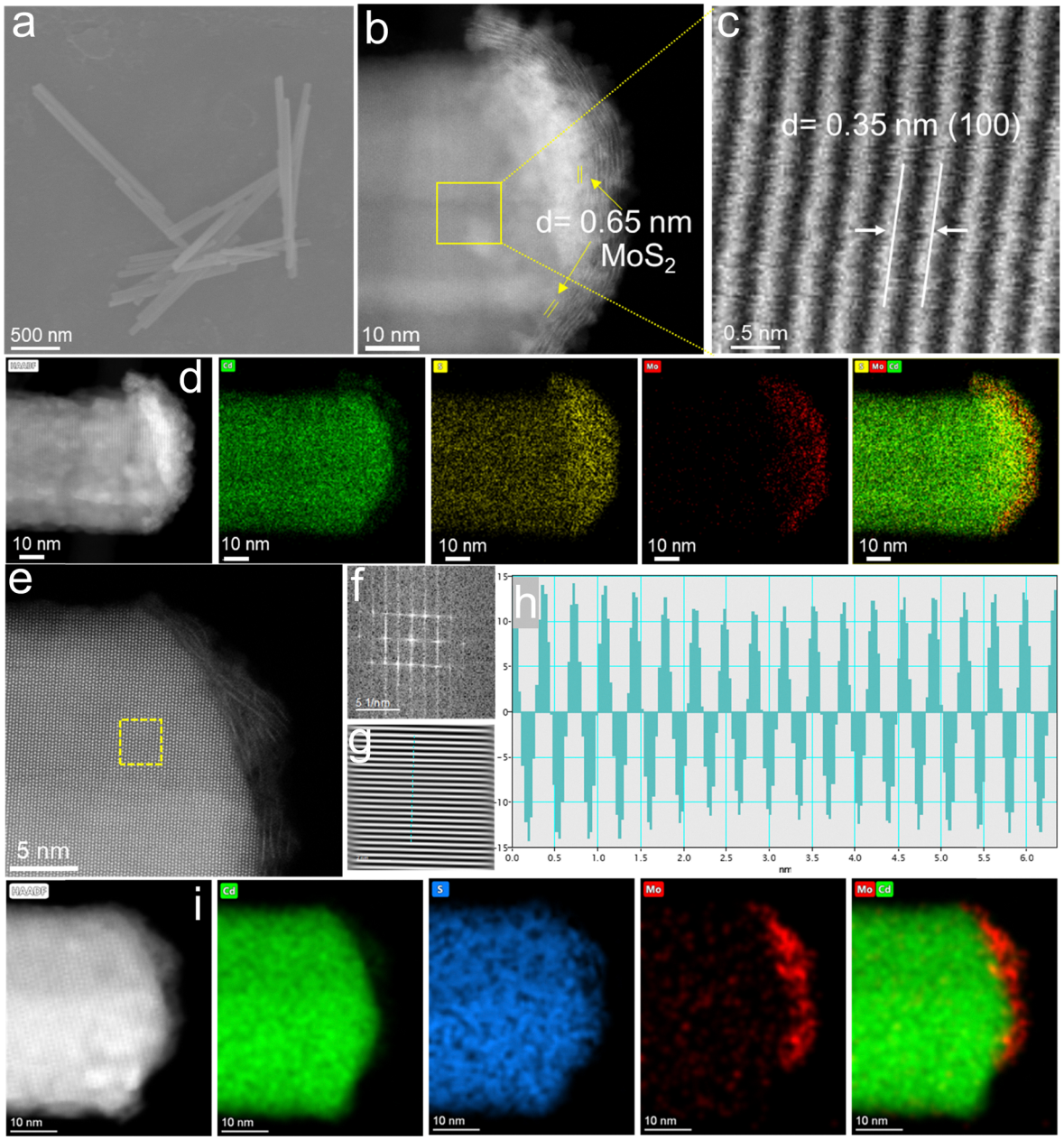

Fig. 1 Morphology of 3-MoS_2/CdS: (a) SEM image, (b), (c) and (e) high-angle annular dark-field scanning transmission electron microscopy (HAADF-STEM) images of 3-MoS_2/CdS. (f) and (g) FFT and inverse FFT of the squared areas in (e), respectively. (h) Line profile across crystal planes shown in (g). (d) and (i) High-angle annular dark field scanning transmission electron microscopy (HAADF-STEM) images and EDS mapping images of a 3-MoS_2/CdS Janus heterojunction for two selected areas.

30 to 40 nm and lengths between 1 and 2 μm. High-resolution transmission electron microscopy (HRTEM) and high-angle annular dark-field scanning transmission electron microscopy (HAADF-STEM) further confirmed the asymmetric 3-MoS_2/CdS heterojunction consisting of amorphous MoS_2 and crystalline CdS with a well-defined interface. The MoS_2 component in the 3-MoS_2/CdS heterojunction displayed a distinct layered structure with an interlayer distance of 0.65 nm at the tips of CdS nanorods (Fig. 1b).[25,26] Additionally, HAADF-STEM images (Fig. 1c and Fig. S2, ESI†), along with fast Fourier transform (FFT) (Fig. 1f), reverse FFT (Fig. 1g) analysis and intensity profiles (Fig. 1h), confirmed the high crystallinity of CdS, characterized by clear lattice fringes of 0.35 nm along the (100) direction.[27] HAADF and energy-dispersive X-ray (EDX) mapping images (Fig. 1d, i and Fig. S2d, ESI†) show an asymmetric distribution of Cd and Mo elements, with Mo species localized at one end of the CdS nanorod. The absence of a distinct gap at the MoS_2/CdS interface indicates the successful formation of the MoS_2/CdS heterostructure with a compact interface.

The crystal structure of synthesized CdS and *x*-MoS_2/CdS samples was analyzed by X-ray diffraction (XRD). As shown in Fig. 2a, all diffraction peaks matched the hexagonal phase of

CdS (PDF# 77-2306), confirming its crystallinity within the *P*63*mc* (186) space group.[28] Notably, no characteristic peaks for MoS_2 were detected in *x*-MoS_2/CdS, likely due to its low concentration, suggesting that MoS_2 does not affect the growth of the CdS crystal structure.[29] The XRD pattern of MoS_2 in Fig. S3 (ESI†) displayed amorphous features, consistent with the layered structures observed in TEM images (Fig. 1b and e).[30]

Inductively coupled plasma mass spectrometry (ICP-MS) analysis further confirmed the low Mo content in 3-MoS_2/CdS, revealing approximately 1.3% Mo loading (Fig. 2b). X-ray photoelectron spectroscopy (XPS) analysis verified the presence of Mo, Cd, and S, which is consistent with the results from EDX analysis. For bare CdS, the Cd $3d_{5/2}$ and Cd $3d_{3/2}$ peaks appeared at 405.7 and 412.6 eV, respectively, while S $2p_{3/2}$ and S $2p_{1/2}$ peaks were observed at 160.9 and 163.2 eV (Fig. 2c and d).[31] With the growth of MoS_2, the Cd peaks shifted positively by 0.8 eV, indicating strong electronic interactions between MoS_2 and CdS in 3-MoS_2/CdS. In contrast, the S $2p_{1/2}$ and S $2p_{3/2}$ peaks of CdS exhibited a notable negative shift of 0.11 eV and 0.67 eV, respectively. Additionally, the Mo 3d peak in 3-MoS_2/CdS shifted to a lower binding energy compared to that in MoS_2 (Fig. S4, ESI†). The decreased binding energy is likely due to a stronger electronic screening effect attributed to the increased electron concentration in MoS_2 in the composites.[32] This interpretation is further supported by XANES analysis (Fig. S5a and b, ESI†), where a slight negative shift at the Cd K-edge and a positive shift with enhanced white-line intensity at the Mo K-edge indicate increased electron density at Cd sites and electron depletion at Mo sites, respectively. These spectral features collectively support the formation of Mo–S–Cd covalent bonds and an asymmetric charge distribution across the interface.[26] Therefore, the 3-MoS_2/CdS heterojunction catalyst established Mo–S–Cd interfacial charge-migration channels, where the BIEF arising from the potential difference of the two components drove electron transfer from CdS to MoS_2 and ensured efficient and directed charge migration.[33]

The photocatalytic performance of the as-prepared samples was evaluated in a 10 vol% lactic acid (LA) solution under visible light irradiation ($\lambda > 420$ nm). The photocatalytic plastic reforming coupled with the HER involves two processes: proton reduction with photoexcited electrons and plastic reforming by oxidative holes. To assess the photocatalytic activity, H_2 production rates were analyzed across different samples. The results reveal that MoS_2 content significantly influences H_2 production for the MoS_2/CdS heterostructure. Pure CdS exhibits a low H_2 production rate of 3.9 mmol g^{-1} h^{-1} due to limited charge carriers' separation and their fast recombination. MoS_2 alone shows no H_2 generation, indicating its lack of photocatalytic activity. Incrementally equipping MoS_2 on CdS significantly improved H_2 production, reaching 73.1 mmol g^{-1} h^{-1} for 1-MoS_2/CdS, 220.4 mmol g^{-1} h^{-1} for 2-MoS_2/CdS, and peaking at 268.7 mmol g^{-1} h^{-1} for 3-MoS_2/CdS (Fig. 3a). This increase is attributed to the formation of a stronger BIEF at the MoS_2/CdS interface, which enhances charge separation and reduces recombination. However, further increasing the MoS_2 content led to decreased H_2 production rates, with 177.4 mmol g^{-1} h^{-1} for 4-MoS_2/CdS and 120.8 mmol g^{-1} h^{-1} for 5-MoS_2/CdS. The decreased HER efficiency is likely due to

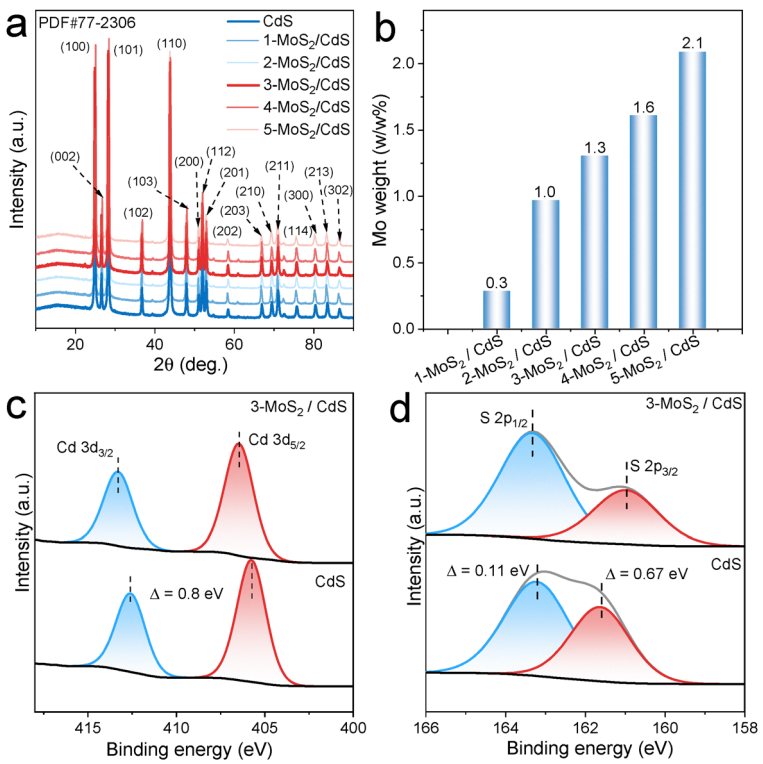

Fig. 2 Characterization of CdS and *x*-MoS_2/CdS. (a) XRD patterns. (b) ICP-MS and XPS spectra of (c) Cd 3d and (d) S 2p for CdS and 3-MoS_2/CdS.

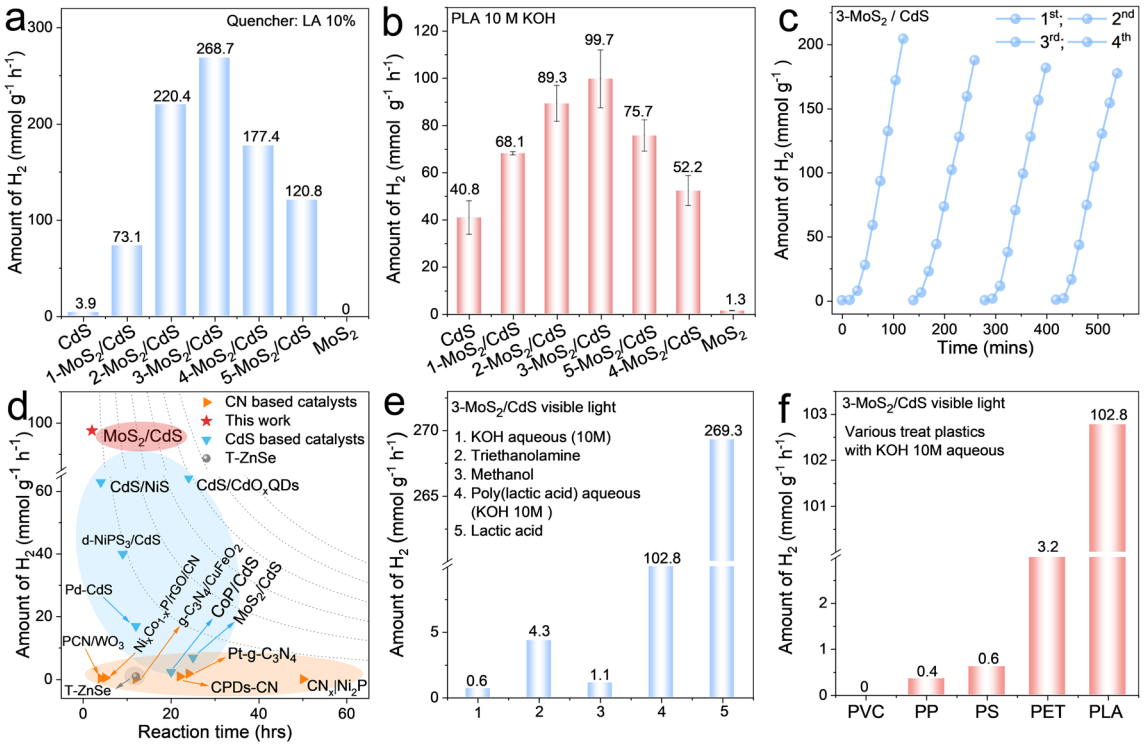

Fig. 3 Performance evaluation of CdS photocatalysts with various doses of MoS_2 tipped on the CdS in PR coupled with HER. (a) PR plastic coupled with the HER in 10 vol% LA solution. (b) PR plastic coupled with the HER in PLA solution (10 M KOH). (c) Cycling experiment of 3-MoS_2/CdS. (d) Comparison of H_2 generation in PR of PLA between 3-MoS_2/CdS and heterojunction catalysts in the literature. (e) Comparison of H_2 generation for 3-MoS_2/CdS using different sacrificial agents in the HER. (f) H_2 generation rate for 3-MoS_2/CdS in plastic reforming coupled with the HER using different pre-treated plastics by 10 M KOH (light source: $\lambda > 420$ nm, reaction time: 2 hours, catalyst: 5 mg, reaction volume: 100 mL).

excessive MoS_2 coverage, which blocks light absorption and decreases photocarrier generation.

Pre-treated PLA in a strong KOH aqueous solution was tested as an alternative sacrificial agent as PLA is hydrolysed into small molecular products. Under identical conditions, H_2 production rates exhibited the same trend as observed with LA as the sacrificial agent, reaching 40.8, 68.1, 89.3, 99.7, 75.7, 52.2, and 1.3 mmol g^{-1} h^{-1} for CdS, 1-MoS_2/CdS, 2-MoS_2/CdS, 3-MoS_2/CdS, 4-MoS_2/CdS, 5-MoS_2/CdS, and MoS_2, respectively (Fig. 3b). These findings highlighted the crucial role of optimized MoS_2/CdS interfaces in achieving efficient photocatalytic HER, as well as confirming that 3-MoS_2/CdS achieved the highest photocatalytic H_2 production using LA or KOH-pretreated PLA solutions as the sacrificial agents. Furthermore, the stability of the 3-MoS_2/CdS catalyst was validated through consistent H_2 yields across multiple cycling tests, as shown in Fig. 3c. A slight reduction in H_2 production with repeated use was observed, likely due to the accumulation of organic compounds on the catalyst surface that block active sites. The 3-MoS_2/CdS catalyst also outperformed the state-of-the-art photocatalysts (Fig. 3d) for H_2 generation in alkaline PLA solutions, under visible light irradiation and without the addition of cocatalyst or additional sacrificial agents.

To investigate the source of H_2 production, we performed a comparative experiment, substituting the same volume of PLA solution with half the volume (50 mL) of deuterium oxide (D_2O) and pure water (H_2O). As shown in Fig. S6a and b (ESI†), diluting the original PLA solution (91.7 mmol g^{-1} h^{-1}) to 50% concentration using an equal volume of D_2O resulted in a reduced H_2 evolution rate of 44.9 mmol g^{-1} h^{-1}, compared to 39.0 mmol g^{-1} h^{-1} when diluted with the same volume of H_2O. When PLA was fully hydrolyzed in D_2O, the H_2 evolution rate further decreased to 19.9 mmol g^{-1} h^{-1} (Fig. S6c, ESI†). These results indicate that both PLA concentration and the nature of the solvent significantly influence photocatalytic H_2 production, with the solvent primarily acting as the proton source.

These results indicate that H_2 is primarily derived from the protons in H_2O rather than from the organic byproducts from PLA. The effect of KOH concentration during PLA pre-treatment on H_2 production was also examined. As depicted in Fig. S7 (ESI†), higher concentrations of KOH significantly enhanced H_2 generation, likely due to more effective breakdown of PLA into monomeric units, thus promoting their interactions with photo-induced holes on a catalyst surface.[34,35] To further confirm the role of plastics in the photocatalytic HER process, a 10 M KOH aqueous solution without PLA was tested, yielding a minimal H_2 generation rate of 0.6 mmol g^{-1} h^{-1}. This outcome highlights the critical role of hydrolysed PLA monomers as electron sacrificers in hole oxidation, facilitating photoreduction of aqueous protons to H_2 on the surface of 3-MoS_2/CdS (Fig. 3e).

Furthermore, photocatalytic experiments demonstrated that 3-MoS_2/CdS achieved significantly higher H_2 production

using pre-treated PLA in a strong alkaline solution compared to conventional sacrificial agents. Specifically, using PLA as the sacrificial agent achieved a H_2 production rate of 102.8 mmol g^{-1} h^{-1}, nearly 100 times higher than that using methanol (1.1 mmol g^{-1} h^{-1}) and 25 times higher than that using triethanolamine (4.3 mmol g^{-1} h^{-1}), both of which are typical electron sacrificers used in the photocatalytic HER. LA yielded the highest H_2 production rate at 269.3 mmol g^{-1} h^{-1} (Fig. 3e). These results underscored the great potential of PLA (and its hydrolyzed product of LA) as a sustainable and effective sacrificial agent for enhanced photocatalytic H_2 production. Additionally, as shown in Fig. 3f, 3-MoS_2/CdS demonstrated higher H_2 generation rates for PR of polyesters (PET and PLA) compared with polyolefins (PVC, PP, and PS), possibly due to the presence of –COO functionalities that activated the C–C backbone in plastics for hole oxidation.

To further understand the interfacial effect of the MoS_2/CdS Janus heterostructure, density functional theory (DFT) calculations were conducted to evaluate the electronic structures of counterparts. Results showed that the work function (Φ) of CdS

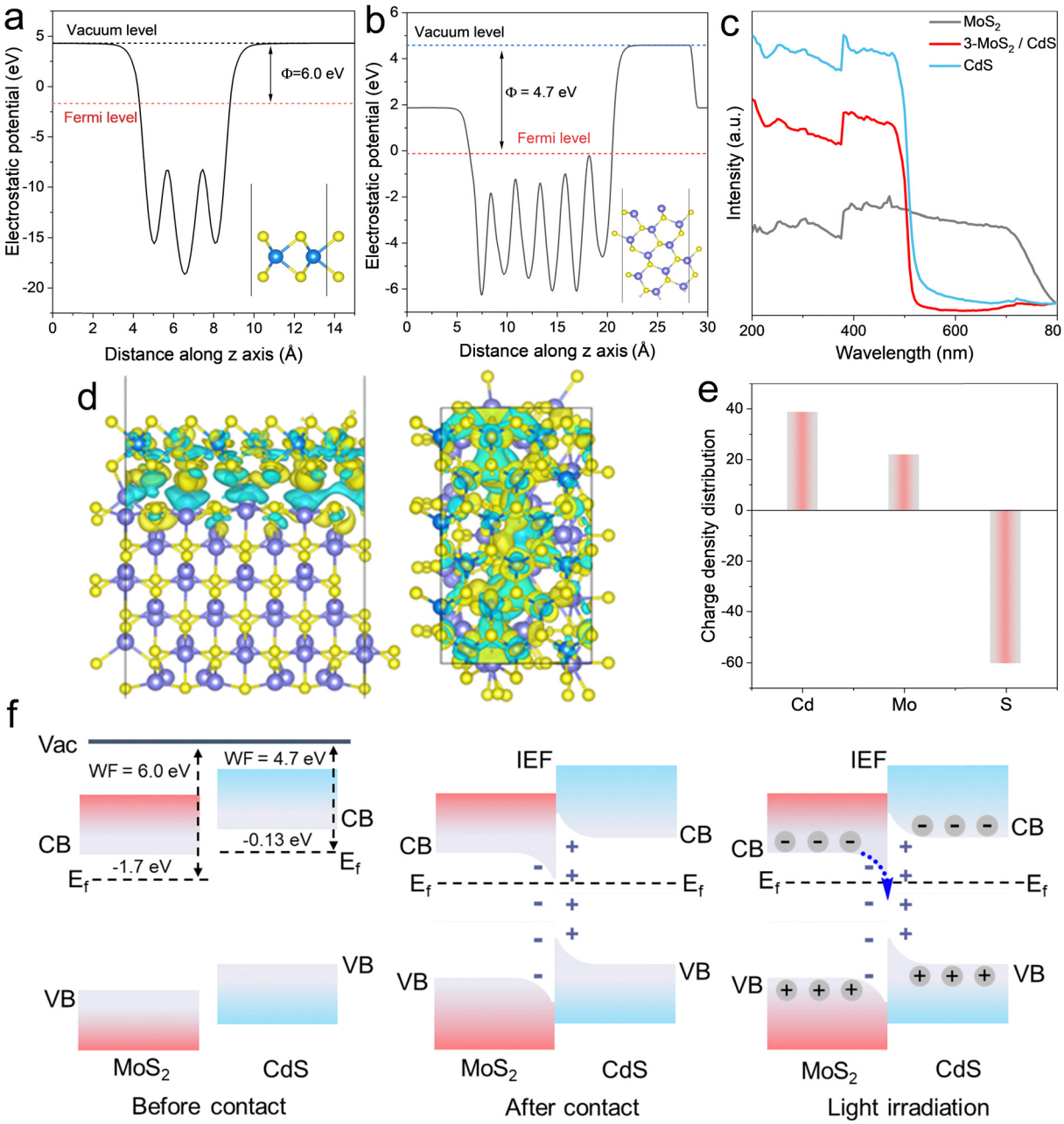

Fig. 4 Work function of (a) MoS_2(002) and (b) CdS (102) surfaces. (c) UV-vis spectra of CdS, MoS_2 and MoS_2/CdS. (d) Charge density difference at the CdS/MoS_2 interface, where the yellow colour represents charge accumulation, and the blue colour refers to the charge depletion. (e) Calculated average charge density distributions for Cd, Mo and S. (f) Schematic illustration of energy band arrangement and the path of photoexcited charge carrier transfer in 3-MoS_2/CdS.

(4.7 eV) was lower than that of MoS_2 (6.0 eV) (Fig. 4a and b), leading to a significantly higher Fermi level (E_f) for CdS (−0.13 eV) compared to MoS_2 (−1.7 eV). This difference in E_f drives electron flow from CdS to MoS_2, positioning MoS_2 as the reductive site and CdS as the oxidative site.[36] Consequently, the Mo–S–Cd interface facilitates charge redistribution and localization, generating spatial potential difference that enhances charge separation and minimizes charge carriers' recombination, thereby boosting photocatalytic performances.

Ultraviolet-visible (UV-vis) diffuse reflectance spectroscopy analysis, illustrated in Fig. 4c, reveals that both CdS and 3-MoS_2/CdS share similar UV-vis absorption profiles, while MoS_2 alone exhibits minimal light absorption. This suggests that light absorption is not the primary factor determining photocatalytic efficiency. Furthermore, the absorption edges of CdS and MoS_2 are comparable, with bandgaps of 2.38 eV and 1.87 eV, respectively, as determined from the Tauc plots (Fig. S8b and f, ESI†). Meanwhile, the bandgaps of 1-MoS_2/CdS, 2-MoS_2/CdS, and 3-MoS_2/CdS are estimated to be 2.36 eV, 2.33 eV, and 1.67 eV, respectively (Fig. S8c–e, ESI†), suggesting that coupling with MoS_2 slightly modulates the bandgap energy of CdS. To further explore the band structures of the catalysts, Mott–Schottky (MS) tests were conducted. As shown in Fig. S9a and b (ESI†), the MS curves exhibit positive slopes for both CdS and MoS_2, confirming their n-type semiconductor characteristics. The flat band potentials (E_{fb}) for CdS and MoS_2 were determined to be −0.82 eV and −0.21 eV relative to the reversible hydrogen electrode (RHE), respectively, which allows for the assessment of their CB positions at −0.82 eV and −0.21 eV accordingly. Thus, the energy band structures for CdS and MoS_2 are summarized in Fig. S10 (ESI†).

Charge density difference and Bader charge analysis further confirmed the electron transfer between CdS and MoS_2 in the 3-MoS_2/CdS heterostructure. Fig. 4d demonstrates that Cd and Mo atoms at the Mo–S–Cd interface tend to lose electrons to interfacial S atoms, supporting the findings from XPS. Such electron transfer results in significant charge accumulation and depletion at the interface, as indicated by the charge density difference, indicating the strong electronic interactions between MoS_2 and CdS, which induce charge redistribution and establish a robust IEF.[37] Additionally, Fig. 4e shows that Cd loses more electrons than Mo, indicating that CdS obtains a higher potential than MoS_2. Consequently, the charge transfer mechanism within the S-scheme junction between CdS and MoS_2 is illustrated in Fig. 4f. When CdS (with a higher E_f) comes into contact with MoS_2 (with a lower E_f), electrons flow from CdS to MoS_2 until the E_f equalization, creating an electron-depleted region on CdS and an electron-rich zone on MoS_2. The resulting IEF from CdS to MoS_2 induces upward band bending in CdS and downward bending in MoS_2.[38] Under visible light irradiation, electron–hole pairs are generated in both CdS and MoS_2; the IEF, combined with band bending and

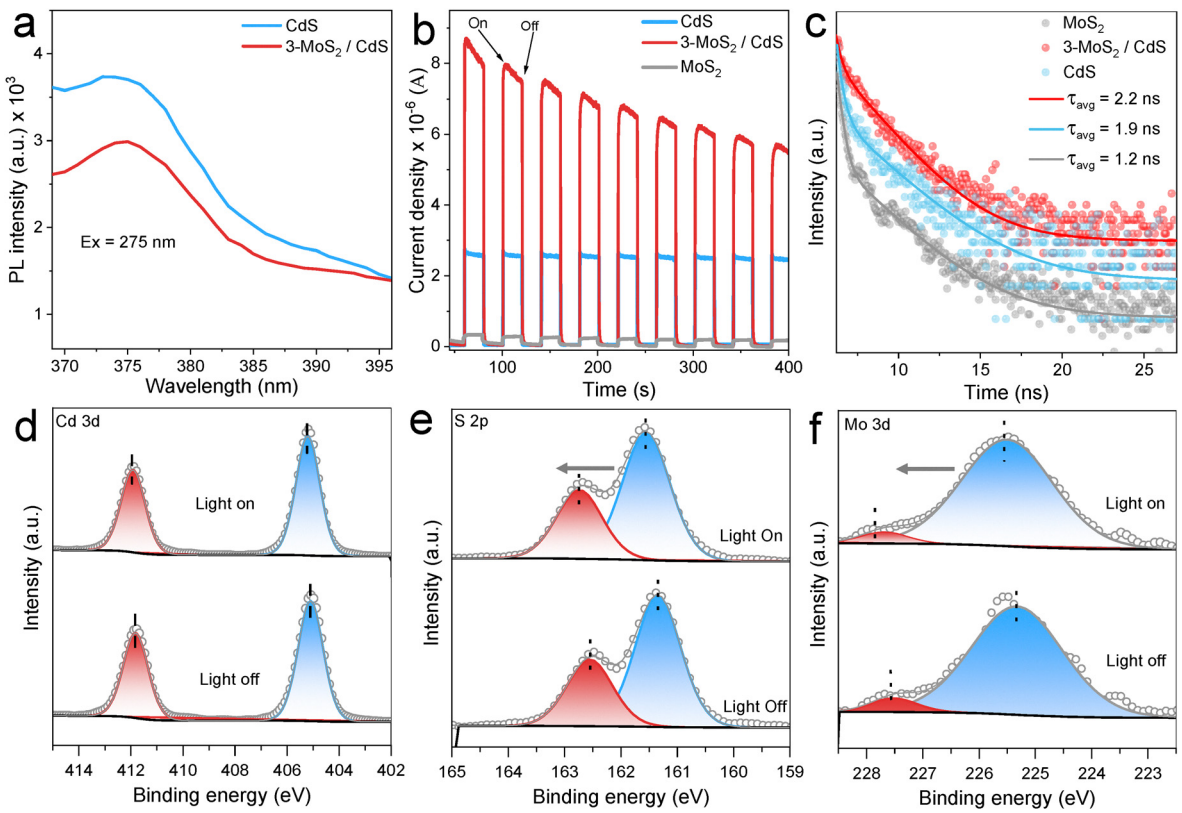

Fig. 5 Characterization of physicochemical properties of CdS, MoS_2 and 3-MoS_2/CdS. (a) Steady PL. (b) Transient photocurrent responses and (c) transient PL spectra. *In situ* irradiated XPS of 3-MoS_2/CdS for (d) Cd 3d. (e) S 2p (f) Mo 3d.

interfacial bonding, drives electrons from the CB of MoS_2 to recombine with holes in the VB of CdS.[17,39] Therefore, the 3-MoS_2/CdS heterojunction exhibits remarkable photocatalytic performance due to its optimized charge separation, migration dynamics, and energy configuration.

Photoelectrochemical properties of as-synthesized samples were further examined to study the influences of photogenerated charge separation and transfer of 3-MoS_2/CdS on photocatalytic H_2 production and PLA reforming. As illustrated in Fig. 5a, photoluminescence (PL) spectra show that pristine CdS, when excited at 275 nm, exhibits a prominent emission peak at around 375 nm, which is higher than that of 3-MoS_2/CdS. The PL intensity was significantly reduced in 3-MoS_2/CdS, indicating a lower electron–hole recombination rate in this configuration. Photocurrent response analysis (Fig. 5b) and electrochemical impedance spectroscopy (EIS) measurements (Fig. S11, ESI†) further confirmed that the established IEF at the Mo–S–Cd interface promoted efficient migration of photogenerated carriers. Thus, CdS photocorrosion is mitigated when coupled with MoS_2, giving rise to improved stability and photocatalytic efficiency. Compared to CdS or MoS_2 alone, the 3-MoS_2/CdS heterostructure exhibits stronger current responses and smaller arc radii, demonstrating superior charge transfer efficiency for surface redox reactions.

Transient absorption spectroscopy in Fig. S12 (ESI†) reveals that MoS_2/CdS exhibits a markedly slower decay and longer carrier lifetimes than pristine CdS, indicating more efficient charge separation and suppressed recombination at the heterojunction interface.[40] Additionally, fluorescence lifetime measurements (Fig. 5c) reveal an average exciton lifetime of 2.2 ns for 3-MoS_2/CdS, which exceeds those of CdS (1.9 ns) and MoS_2 (1.2 ns), suggesting that IEF effectively suppresses charge recombination and extends exciton lifetime within 3-MoS_2/CdS. These findings imply that the 3-MoS_2/CdS heterostructure forms Mo–S–Cd channels that facilitate electron transport, lower charge transfer resistance, and reduce recombination of photogenerated charges. *In situ* light-irradiated XPS was conducted to further investigate carrier transfer behavior. As illustrated in Fig. 5d and f, the Cd 3d peaks of 3-MoS_2/CdS remain unchanged under light exposure, while S 2p and Mo 3d peaks shift to higher binding energies. These shifts imply that photogenerated electrons are transferred from the CB of MoS_2 to the VB of CdS.[41] This interfacial electron–hole recombination process aligns with the mechanism depicted in Fig. 4f, where the IEF at the Mo–S–Cd interface ensures efficient electron

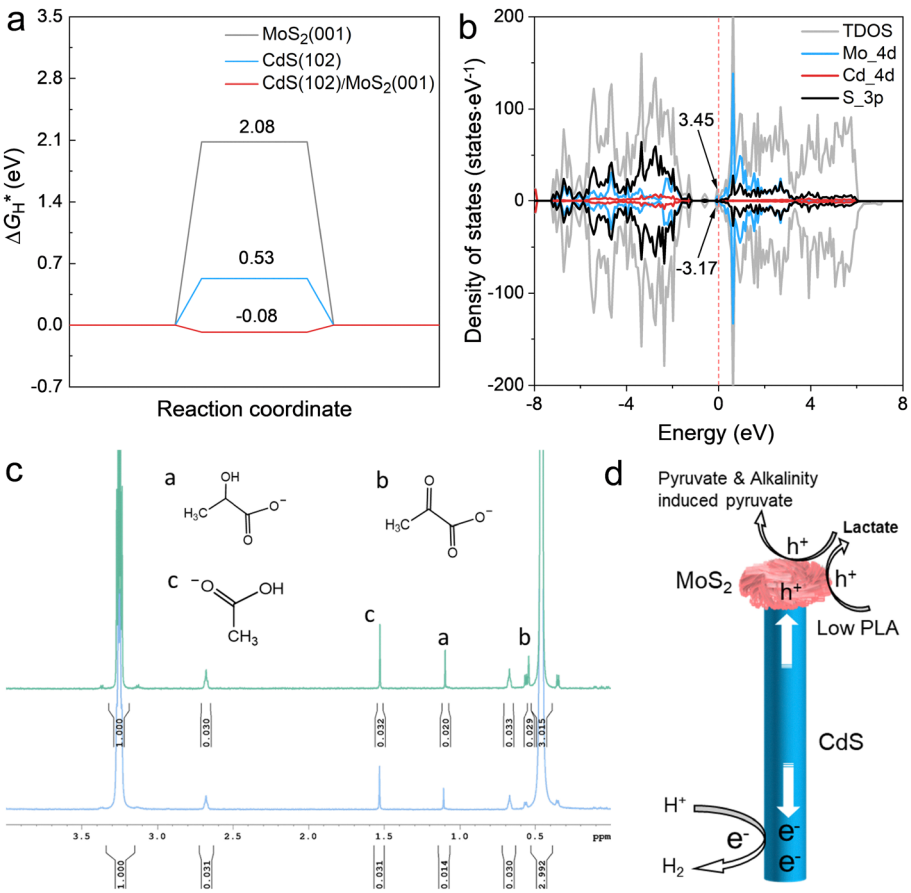

Fig. 6 (a) Simulated H adsorption free energy of H (ΔG_H^*) for MoS_2(002), CdS(102), and 3-MoS_2/CdS interface. (b) Density of states of the 3-MoS_2/CdS interface. (c) ^{1}H NMR spectra of substrates of PLA pre-treated in 10 M KOH (lower) and after 2 hours PR (upper). (d) Schematic mechanisms for charge transfer in 3-MoS_2/CdS and PR plastic recycling coupled with the HER.

utilization, thereby enhancing photoreduction of protons to yield H_2 on the surface of CdS and hole-driven oxidation of PLA on MoS_2.

DFT calculations were conducted to investigate the thermodynamic properties, specifically the Gibbs free energy (ΔG), for the photocatalytic HER. As illustrated in Fig. 6a, the calculated ΔG_H^* at the 3-CdS/MoS_2 interface is −0.08 eV, which is significantly lower than that of pure CdS (0.53 eV) and MoS_2 (2.08 eV). This finding indicates that the 3-CdS/MoS_2 heterostructure possesses improved adsorption/desorption characteristics and enhanced HER activity compared to CdS and MoS_2 alone.[15,16] Fig. 6b further illustrates that, near the E_f level, Mo 4d orbitals filled the occupied states, contributing to high electrical conductivity at the interface. This indicates that Mo plays a crucial role in mediating charge transport during photocatalytic processes.[18,19]

In addition to H_2 as the reductive product, the liquid products generated from the PR reaction were analyzed using proton nuclear magnetic resonance (^{1}H NMR) spectroscopy (Fig. 6c). The analysis confirmed that PLA was hydrolyzed in the KOH solution into smaller organic molecules, including lactate (labelled as a) and acetate (labelled as c),[20,30] prior to the photocatalytic reaction. After two hours of PR, a new primary product, pyruvate or alkalinity-induced pyruvate (labelled as b),[2] was detected, indicating further transformation of PLA hydrolysis products during the photocatalytic process. Additionally, the results of liquid chromatography-mass spectrometry (LC-MS) (Fig. S13, ESI†) revealed the formation of low molecular weight polymers and lactate (89 m/z) from PLA degradation. An increased concentration of lactate and a noticeable decrease in PLA were observed after two hours of photocatalysis (Fig. S13, ESI†),[30] indicating that PLA was oxidized into smaller organic molecules without detection of CO and CO_2 (Fig. S14, ESI†). Moreover, the LA content in solution was quantified before and after the reaction, with the results (Fig. S15, ESI†) showing an increase from 3.9 mg to 4.4 mg, further confirming the accumulation of lactate species during the reaction.

Under anaerobic conditions, since the lower VB energy (1.66 V) of MoS_2 is insufficient to generate hydroxyl radicals from water ($^\bullet$OH/H_2O = 2.8 V), the oxidative holes on MoS_2 dominate PLA oxidation and secure continuous charge carrier (h^+) consumption. The charge transfer mechanism for the 3-CdS/MoS_2 catalyst is illustrated in Fig. 6d. Hydrolysates from low molecular weight PLA serve as electron donors, and surface holes on MoS_2 oxidize these hydrolysates primarily into LA and pyruvate, along with other oxidized products. Partial LA undergoes further oxidation to pyruvate. Simultaneously, photo-induced electrons on CdS reduce protons to generate H_2. The interfacial IEF-directed charge separation and transfer, collaborated with spatially separated hydrolysate oxidation and HER, enables high photocatalytic performance of 3-MoS_2/CdS in synergistic H_2 generation and PLA reforming.

4. Conclusion

This study successfully developed an asymmetric MoS_2/CdS heterojunction catalyst through a one-pot solvothermal method. The strong Mo–S–Cd interactions at the interface generated a strong internal electric field, significantly enhancing charge separation and boosting photocatalytic efficiency. Also, the asymmetric heterostructure greatly improves HER thermodynamics on CdS and PLA oxidation on MoS_2, achieving an exceptional H_2 production rate of 97.7 mmol g^{-1} h^{-1} without any cocatalysts or sacrificial agents. Furthermore, the strengthened charge dynamics facilitated PLA reforming, selectively converting waste PLA into valuable chemicals such as lactate and pyruvate. These findings highlight the great potential of the asymmetric MoS_2/CdS photocatalyst for sustainable H_2 production and plastic waste recycling, presenting an eco-friendly alternative to conventional plastic disposal methods.

Conflicts of interest

There are no conflicts to declare.

Data availability

All data underpinning this study, including processed XRD, XPS, UV-vis DRS, PL, EIS and photocurrent data; TEM/HRTEM/HAADF-STEM micrographs; photocatalytic H_2-evolution and plastic-reforming data; and the DFT computations, are provided in the manuscript and ESI.† No software or code have been included, and no human or animal data were generated.

Acknowledgements

The authors acknowledge the financial support from the Australian Research Council (DP230102406, FT230100526, and LE230100168). The simulations were conducted using resources and services provided by the National Computational Infrastructure (NCI) (project code: aj92).

References

1 K. S. Hu, Y. Y. Yang, Y. X. Wang, X. G. Duan and S. B. Wang, *Chem. Catal.*, 2022, **2**, 724–761.
2 T. Uekert, M. F. Kuehnel, D. W. Wakerley and E. Reisner, *Energy Environ. Sci.*, 2018, **11**, 2853–2857.
3 K. F. Wu, Z. Y. Chen, H. J. Lv, H. M. Zhu, C. L. Hill and T. Q. Lian, *J. Am. Chem. Soc.*, 2014, **136**, 7708–7716.
4 F. T. He, Y. M. Lu, Y. Z. Wu, S. L. Wang, Y. Zhang, P. Dong, Y. Q. Wang, C. C. Zhao, S. J. Wang, J. Q. Zhang and S. B. Wang, *Adv. Mater.*, 2024, **36**(9), 2307490.
5 X. Wang, B. Y. Liu, S. Q. Ma, Y. J. Zhang, L. Z. Wang, G. Q. Zhu, W. Huang and S. C. Wang, *Nat. Commun.*, 2024, **15**(1), 2600.
6 K. F. Wu, H. M. Zhu and T. Q. Lian, *Acc. Chem. Res.*, 2015, **48**, 851–859.
7 Q. C. Yuan, D. Liu, N. Zhang, W. Ye, H. X. Ju, L. Shi, R. Long, J. F. Zhu and Y. J. Xiong, *Angew. Chem., Int. Ed.*, 2017, **56**, 4206–4210.
8 T. Han, X. Cao, K. A. Sun, Q. Peng, C. L. Ye, A. J. Huang, W. C. Cheong, Z. Chen, R. Lin, D. Zhao, X. Tan, Z. W. Zhuang,

C. Chen, D. S. Wang and Y. D. Li, *Nat. Commun.*, 2021, **12**(1), 4952.
9 C. M. Wolff, P. D. Frischmann, M. Schulze, B. J. Bohn, R. Wein, P. Livadas, M. T. Carlson, F. Jäckel, J. Feldmann, F. Würthner and J. K. Stolarczyk, *Nat. Energy*, 2018, **3**, 862–869.
10 Z. J. Zhu, H. W. Huang, L. Z. Liu, F. Chen, N. Tian, Y. H. Zhang and H. Yu, *Angew. Chem., Int. Ed.*, 2022, **61**(26), e202203519.
11 C. Han, Z. K. Zeng, X. R. Zhang, Y. J. Liang, B. K. Kundu, L. Yuan, C. L. Tan, Y. Zhang and Y. J. Xu, *Angew. Chem., Int. Ed.*, 2024, **63**(38), e202408527.
12 C. B. Bie, B. C. Zhu, L. X. Wang, H. G. Yu, C. H. Jiang, T. Chen and J. G. Yu, *Angew. Chem., Int. Ed.*, 2022, **61**(44), e202212045.
13 C. X. Liu, K. S. Liu, Y. J. Xu, Z. Wang, Y. X. Weng, F. L. Liu and Y. Chen, *Angew. Chem., Int. Ed.*, 2024, **63**(16), e202401255.
14 J. Y. Li, C. L. Tan, M. Y. Qi, Z. R. Tang and Y. J. Xu, *Angew. Chem., Int. Ed.*, 2023, **62**, e202303054.
15 G. Kresse and J. Furthmuller, *Phys. Rev. B: Condens. Matter Mater. Phys.*, 1996, **54**, 11169–11186.
16 J. P. Perdew, K. Burke and M. Ernzerhof, *Phys. Rev. Lett.*, 1996, **77**, 3865–3868.
17 G. Kresse and J. Furthmuller, *Comput. Mater. Sci.*, 1996, **6**, 15–50.
18 P. P. Zhang, X. Wang, Y. Y. Yang, H. F. Yang, C. S. Lu, M. R. Su, Y. Zhou, A. C. Dou, X. W. Li, X. C. Hou and Y. J. Liu, *J. Colloid Interface Sci.*, 2024, **655**, 383–393.
19 J. J. Liu, B. Cheng and J. G. Yu, *Phys. Chem. Chem. Phys.*, 2016, **18**, 31175–31183.
20 J. Y. Kim, H. Park, W. Joo, D. H. Nam, S. Lee, H. G. Kim, I. K. Ahn, H. Y. Kang, G. B. Lee, I. H. Jung, M. Y. Kim, G. D. Lee and Y. C. Joo, *J. Mater. Chem. A*, 2019, **7**, 7451–7458.
21 Y. You, P. Han, S. Song, W. Luo, S. Zhao, K. Han, Y. Tian, N. Yan and X. Li, *Angew. Chem., Int. Ed.*, 2023, **62**, e202306452.
22 J. Li, G. Zhan, Y. Yu and L. Zhang, *Nat. Commun.*, 2016, **7**, 11480.
23 W. J. Xu, J. Jia, T. Wang, C. Li, B. W. He, J. P. Zong, Y. W. Wang, H. J. Fan, H. X. Xu, Y. H. Feng and H. Y. Chen, *Angew. Chem., Int. Ed.*, 2020, **59**, 22246–22251.
24 G. Nie, L. Xiao, J. X. Bi, S. B. Wang and X. G. Duan, *Appl. Catal., B*, 2022, **315**, 121584.
25 S. Zhang, H. B. Li, L. Wang, J. D. Liu, G. J. Liang, K. Davey, J. R. Ran and S. Z. Qiao, *J. Am. Chem. Soc.*, 2023, **145**, 6410–6419.
26 S. G. Liu, Z. J. Li, Y. X. Chang, M. G. Kim, H. Jang, J. Cho, L. Q. Hou and X. Liu, *Angew. Chem., Int. Ed.*, 2024, **63**(12), e202400069.
27 J. Hu, B. Li, X. Li, T. Yang, X. Yang, J. Qu, Y. Cai, H. Yang and Z. Lin, *Adv. Mater.*, 2024, **36**, e2412070.
28 Y. K. Zhang and Z. L. Jin, *Catal. Sci. Technol.*, 2019, **9**, 1944–1960.
29 M. M. Du, Y. Zhang, S. L. Kang, X. Y. Guo, Y. X. Ma, M. Y. Xing, Y. Zhu, Y. Chai and B. C. Qiu, *ACS Catal.*, 2022, **12**, 12823–12832.
30 T. Uekert, H. Kasap and E. Reisner, *J. Am. Chem. Soc.*, 2019, **141**, 15201–15210.
31 J. Wang, Y. Q. Zhang, S. J. Jiang, C. Z. Sun and S. Q. Song, *Angew. Chem., Int. Ed.*, 2023, **62**(35), e202307808.
32 T. Sun, S. Li, L. Zhang and Y. X. Xu, *Angew. Chem., Int. Ed.*, 2023, **62**(27), e202301865.
33 S. K. Xue, H. Tang, M. Shen, X. C. Liang, X. Y. Li, W. D. Xing, C. Yang and Z. Y. Yu, *Adv. Mater.*, 2024, **36**(16), 2311937.
34 Y. Zhang, N. Cao, X. M. Liu, F. T. He, Y. M. Lu, S. L. Wang, C. C. Zhao, Y. Q. Wang, J. Q. Zhang and S. B. Wang, *ACS Catal.*, 2024, **14**, 13768–13780.
35 Z. X. Wu, P. F. Yang, Q. C. Li, W. P. Xiao, Z. J. Li, G. R. Xu, F. S. Liu, B. H. Jia, T. Y. Ma, S. H. Feng and L. Wang, *Angew. Chem., Int. Ed.*, 2023, **62**(14), e202300406.
36 N. Liu, J. L. Jiang, Z. H. Chen, B. Y. Wu, S. Q. Zhang, Y. Q. Zhang, P. Cheng and W. Shi, *Angew. Chem., Int. Ed.*, 2023, **62**(47), e202312306.
37 R. J. Feng, K. W. Wan, X. Y. Sui, N. Zhao, H. X. Li, W. Y. Lei, J. G. Yu, X. F. Liu, X. H. Shi, M. L. Zhai, G. Liu, H. Wang, L. R. Zheng and M. H. Liu, *Nano Today*, 2021, **37**, 101080.
38 C. Yang, X. Li, M. Li, G. J. Liang and Z. L. Jin, *Chin. J. Catal.*, 2024, **56**, 88–103.
39 M. Li, H. Li, H. F. Fan, Q. F. Liu, Z. Yan, A. Q. Wang, B. Yang and E. R. Wang, *Nat. Commun.*, 2024, **15**(1), 6154.
40 X. L. Wu, S. Liu, Y. Li, M. J. Yan, H. J. Lin, J. R. Chen, S. J. Liu, S. B. Wang and X. G. Duan, *Angew. Chem., Int. Ed.*, 2023, **62**, e202305639.
41 X. Y. Miao, H. Yang, J. He, J. Wang and Z. L. Jin, *Acta Phys. Chim. Sin.*, 2025, **41**, 100051.